Numerical Simulation of the Process of Tunnel Approaching Karst Cave Considering Fluid-Solid Coupling

Ran Xu, Qigui Yang*, Xiaokang Shao

Changjiang Survey, Planning, Design and Research Co., Ltd., Wuhan 430010, China
*yangqigui@cjwsjy.com.cn

Abstract. It is generally believed that under the combined effects of construction disturbance and high water pressure, the collapse or hydraulic fracturing of anti-inrush rock masses between tunnels and unfavorable geological structures constitutes the primary factor inducing water inrush accidents. Consequently, investigating the instability mechanism of anti-inrush rock masses holds significant importance for tunnel construction. Taking the Qinhe Tunnel of the Dianzhong Water Diversion Project as the engineering background, this study establishes a mathematical model for the instability failure of anti-inrush rock masses during tunnel approach toward water-rich karst caves. Utilizing Comsol software, the dynamic evolution patterns of stress fields and seepage fields in surrounding rock during the tunnel's approach to water-rich karst caves are simulated and analyzed. The research findings indicate that: At 7.5 meters from the karst cave, the plastic zone connects to form a water inrush conduit, defining the minimum safety threshold; Displacement exhibits three-stage mutation; Seepage velocity evolves asymmetrically, forming concentrated channels and high-velocity zones near the cave; Permeability coefficient peaks at the critical distance due to pore reorganization, then mutates from localized pathways. This research provides theoretical support for water inrush prevention and safety rock plate design in karst tunnels.

Keywords: Tunnel Engineering; Karst cave; Water Inrush; Fluid-Solid Coupling

1 Introduction

During tunnel excavation, the risk of water and mud inrush significantly increases when tunnels approach karst caves. This hazard is primarily induced by two geological factors: the occurrence characteristics of karst caves and their spatial proximity to tunnels, as well as the fluid-solid coupling mechanism underlying cavity instability under groundwater seepage-stress interaction [1]. Despite considerable advancements in karst geological disaster research, studies on the fluid-solid coupling response of surrounding rock during tunnel construction near karst caves remain insufficient, particularly regarding the systematic analysis of multi-field dynamic evolution during the progressive approach of tunnels toward hidden caves [2]. In recent years, as un-

Y. Liu et al. (eds.), *Proceedings of the 2025 2nd International Conference on Civil Engineering Structures and Concrete Materials (CESCM 2025)*, Advances in Engineering Research 288,
https://doi.org/10.2991/978-94-6463-932-2_12

derground engineering extends into deep karst regions, water inrush disasters caused by interactions between tunnels and buried karst caves have surged, becoming a critical scientific challenge for tunnel safety construction [3].

The geological environment of karst caves is highly heterogeneous and dynamically evolving, forming a complex geo-hydrological coupling system characterized by cavity scale, fracture network connectivity, and groundwater activity [4]. As tunnels gradually approach karst caves, stress redistribution in surrounding rock interacts with sudden seepage field changes, rendering traditional static analysis methods inadequate for capturing catastrophic precursors under fluid-solid coupling effects. Numerical simulation technology provides a vital tool for unraveling the dynamic interaction mechanisms within tunnel-karst systems. By constructing coupled models of stress-seepage-damage fields, it enables full-process simulation from micro-fracture propagation to macro-catastrophic instability, offering breakthrough value for investigating karst water inrush mechanisms [5,6]. While scholars have attempted multi-physics coupling methods to analyze the stability of buried caves during tunnel excavation, further exploration is needed regarding the dynamic response patterns of fluid-solid coupling effects during the progressive approach of tunnels toward karst caves [7,8].

This study, based on a typical karst tunnel engineering case, establishes a mathematical model considering fluid-solid coupling effects for the interaction between tunnels and karst caves. Utilizing the Comsol platform, it simulates the spatiotemporal evolution characteristics of stress, seepage, and displacement fields in surrounding rock during the critical approach phase of tunnels toward karst caves. The research focuses on revealing the controlling mechanisms of fluid-solid coupling on the formation of water inrush pathways and catastrophic mutations. The findings provide theoretical support for dynamic risk assessment of deep-buried karst tunnels and scientific guidance for optimizing construction schemes and disaster prevention in tunnel projects approaching karst cave zones.

2 Fluid-Solid Coupling Model

The analytical framework for fluid-solid coupling in tunnel water inrush hazards comprises two core modules: seepage behavior modeling and rock mass deformation analysis. As illustrated in the proposed multi-physics coupling conceptual framework (Fig.1), numerical implementation is achieved through COMSOL's Fluid Flow and Solid Mechanics modules.

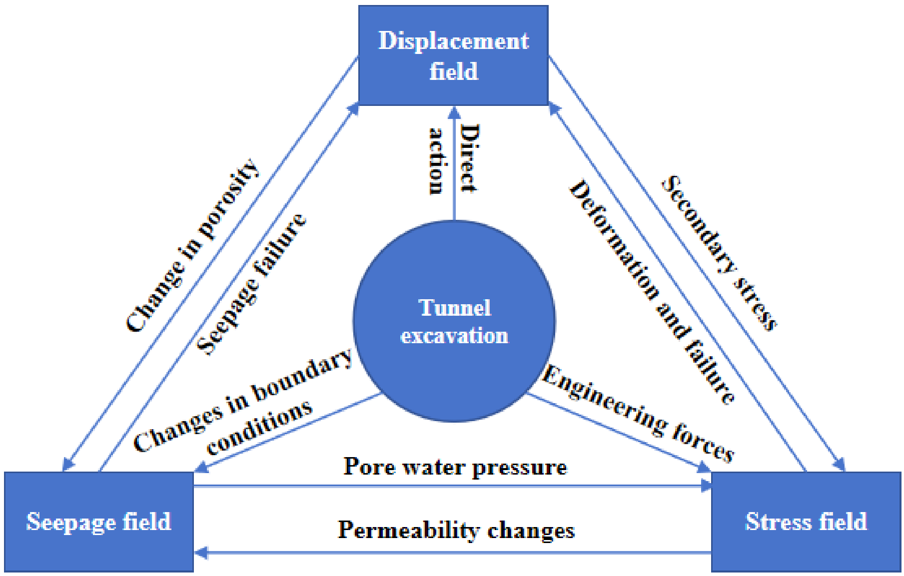

Fig. 1. Conceptual model for multi-field coupling of tunnel water inrush.

In the numerical formulation, the geological medium is idealized as a homogeneous isotropic continuum, with the fluid treated as an incompressible single-phase fluid governed by Darcy's law. Thermal effects on medium deformation are neglected, assuming isothermal seepage conditions. Based on classical effective stress theory, the governing coupled equations for seepage-stress interaction are established as:

$$-\nabla \cdot \sigma = F_v, \quad \sigma = s \tag{1}$$

$$s - S_0 = C:(\varepsilon - \varepsilon_0 - \varepsilon_{inel}) + \left(trace(C:(\varepsilon - \varepsilon_0 - \varepsilon_{inel})/3 + p_w)\right) + \alpha_B p_f \tag{2}$$

$$\varepsilon = \frac{1}{2}[(\nabla u)^T + \nabla u] \tag{3}$$

$$\rho S \frac{\partial p_f}{\partial t} + \nabla \cdot (\rho u) = Q_m - \rho \alpha_B \frac{\partial e_{vol}}{\partial t} \tag{4}$$

$$u = -\frac{k}{\mu}(\nabla p_f + \rho g \nabla D) \tag{5}$$

$$S = \varepsilon_p \chi_f \tag{6}$$

where F_v denotes volumetric force load (N/m^3); σ represents the stress tensor field; u signifies displacement vector field; p_w and p_f correspond to pore fluid pressure and total pressure (Pa), respectively; α_B is Biot's consolidation coefficient; χ defines fluid compressibility (1/Pa); μ indicates dynamic viscosity coefficient of the fluid (Pa·s); and k represents intrinsic permeability (m^2).

Following the parameter evolution model developed by Ji et al. [9], the quantitative relationships between porosity (Φ), permeability (K), and effective stress (σ') are formulated as:

$$\phi = \Phi_0 e^{-a\sigma'}, \quad K = K_0 e^{-b\sigma'} \tag{7}$$

where a and b are empirical fitting parameters, taking values of 1.5×10^{-7} Pa^{-1} and 1.0×10^{-7} Pa^{-1} respectively in this study; Φ_0 and K_0 denote reference porosity and permeability values under initial conditions.

3 Establishment of Tunnel Water Inrush Model

3.1 Project Overview

This study investigates the water inrush mechanisms during tunnel excavation approaching water-rich karst caves, using the karst cave (Figure 2) at DL I 68+347 of the Qinhe Tunnel in the Central Yunnan Water Diversion Project as engineering context. The Qinhe Tunnel connects to the Yanqing Village buried culvert in the northern section and interfaces with the Beiya Tunnel in the southern section, spanning a total length of 20.881 km. The tunnel alignment predominantly follows the eastern slope of Mount Ma'er. At DLI68+347, the tunnel face encounters surrounding rock composed of dolomitic limestone and limestone from the Upper Beiya Formation (Middle Triassic Series), characterized by gently inclined strata, moderate to weak karstic weathering, and relatively developed fissures. The tunnel face was classified as Category V surrounding rock, indicating poor stability with localized risks of rockfall and crown collapse. As the tunnel is situated below the groundwater table, there exists potential for water seepage and inrush when encountering fracture zones or karst caves.

(a) (b)

Fig. 2. Karst cave at DL I 68+347 of Qinhe Tunnel.

On March 21, 2023, a karst cave was discovered on the left side of the tunnel face at DLI68+347 of the Qinhe Tunnel (Figure 2 (a)). The cave had an approximate diameter of 10 meters and contained fill materials of unforeseeable vertical extent, with a burial depth of approximately 220 meters. Corresponding to this subsurface feature, a collapsed cavity measuring approximately 10 meters in diameter and 7 meters in depth was observed on the ground surface above, though the surrounding area was uninhabited (Figure 2 (b)).

3.2 Numerical Model

A numerical model was established based on the Qinhe Tunnel's dimensions and surrounding rock conditions. The computational model measures 120×60×80 m, featuring a horseshoe-shaped cross-section with a height and width of 11.24 m each. The model's coordinate origin is located at the center of the tunnel cross-section at y=0 m. The entire calculation region was discretized into 9152 tetrahedral elements, as depicted in Figure 3.

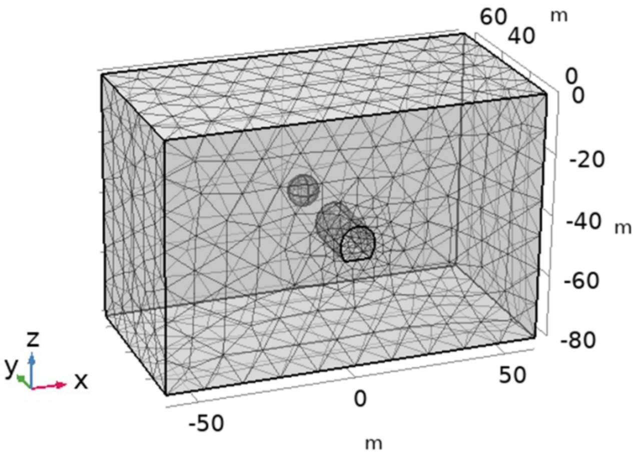

Fig. 3. Water Inrush at DL I 68+347 of Qinhe Tunnel.

The weight of overlying rock-soil mass was converted into in-situ stress (σ x=4.6 MPa, σ y=2.9 MPa, σ z=3.7 MPa) and applied to the model's boundary according to tunnel burial depth. Displacement constraints were imposed on the lateral (left/right/front/rear) boundaries, while the lower boundary was set as fixed and the upper boundary remained free. The karst cave was simplified as a sphere with a diameter of 10 m, with an internal hydrostatic pressure of 2 MPa applied.

This study primarily focuses on the process and mechanisms of water inrush in karst tunnels, with certain simplifications made to the excavation simulation. The tunnel excavation was modeled using the full-face excavation method with a step length of 0.5 m. The selection of computational parameters primarily references the research conducted by Fu [10], with detailed values presented in Table 1.

Table 1. Physical and Mechanical Parameter Values for Surrounding Rock.

Material	Elastic modulus (GPa)	Unit weight (kN/m^3)	Poisson's ratio	Friction angle (^{0})	Cohesion (MPa)	Φ_0	K_0 (cm/s)
Surrounding rock	1.1	21.0	0.15	28.8	1.2	0.2	9.8e-5

4 Calculation Results and Analysis

4.1 Plastic Zone Distribution

This study documents the evolutionary characteristics of plastic zones in surrounding rock at various excavation stages, with relevant nephograms presented in Figure 4. The red-colored regions in these figures represent areas of plastic deformation within the rock mass. Analysis indicates that when the excavation face advances to a position 7.5 meters from the karst cave boundary, the plastic deformation zone ahead of the tunnel face begins to percolate towards and establish connectivity with the cave. This geological connection creates a high-risk conduit for water inrush disasters, as the rock mass acting as a water-resisting barrier at this stage has already lost its structural integrity. Numerical simulation results demonstrates that this critical distance (i.e., the axial spacing between the tunnel face and the karst cave) defines the minimum safe thickness threshold for the water-resisting rock mass. Quantitative analysis confirms this critical safety distance to be 7.5 meters.

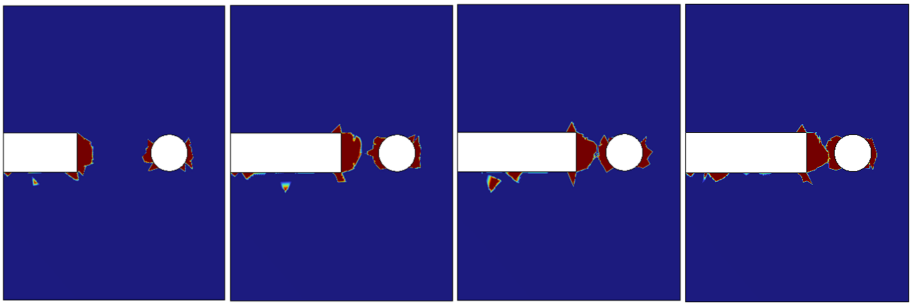

(a) 20m from karst cave (b) 10m from karst cave (c) 8m from karst cave (d) 7.5m from karst cave

Fig. 4. Nephogram of Plastic Zone Distribution at Different Excavation Steps.

To further verify the numerical stability of the critical distance, this study supplemented with a refined simulation using a 15520-element mesh (Fig.5). Through comparative analysis of computational results under varying mesh densities, it was found that when employing 15520 tetrahedral elements for discrete modeling of the anti-inrush rock mass, the critical axial spacing (7.5 m) at which plastic zone penetration occurs between the tunnel face and karst boundary demonstrated strong consistency with calculations from the coarse mesh model (9152 elements), thereby validating the mesh convergence of numerical simulations.

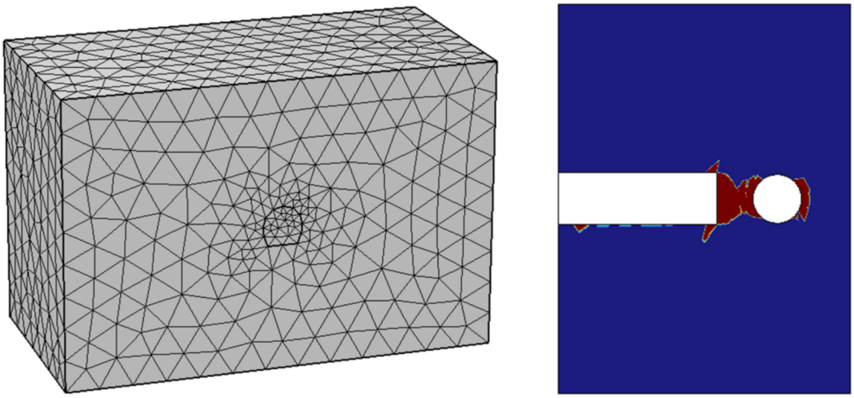

(a)Model (b) Critical Distance 7.5m

Fig. 5. Convergence Validation of Critical Distance Under 15520-Element Mesh.

To investigate the influence of water pressure conditions on the plastic zone expansion, this study conducted numerical simulations under karst cave water pressures of 1.5 MPa and 2.5 MPa while maintaining the critical 7.5 m thickness of the water-resisting rock mass. Results show: At 1.5 MPa karst water pressure, when the tunnel excavation reaches the critical distance of 7.5 m, the plastic deformation zone is smaller than that under 2.0 MPa conditions, and does not connect with the cavern boundary (Fig. 6a); When water pressure increases to 2.5 MPa, the plastic zone extent becomes larger than the reference case (Fig. 6c). This water pressure dependency indicates that karst water pressure significantly intensifies the reduction of rock mass effective stress and plastic flow by enhancing pore water pressure gradients. The calculation results mechanically validate the necessity of pre-drainage pressure reduction measures.

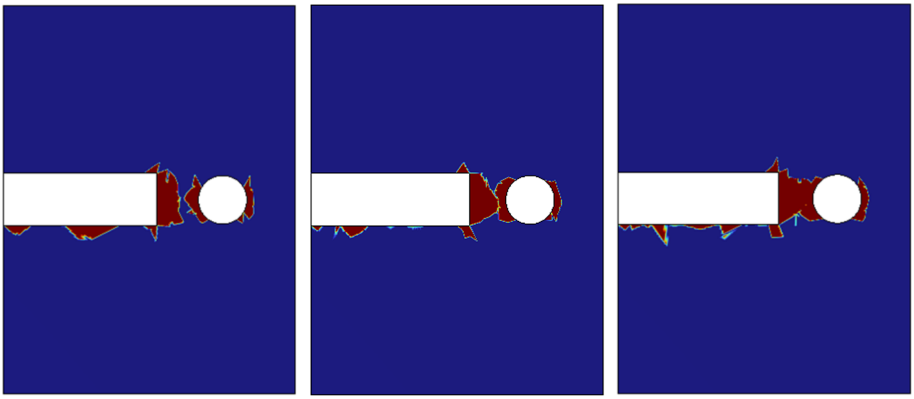

(a)Pore water pressure 1.5MPa (b)Pore water pressure 2.0MPa (c)Pore water pressure 2.5MPa

Fig. 6. Plastic Zone Distribution Under Different Water Pressures.

To investigate the influence mechanism of rock mass cohesion on the critical safety distance, this study conducted numerical simulations under two additional rock mass cohesion conditions (0.8 MPa and 1.6 MPa) based on the baseline case (Fig. 7). In Figure 7, C denotes cohesion, and L represents the critical safety distance. The analysis reveals: When rock mass cohesion decreases to 0.8 MPa, the critical safety distance of the water-resisting rock mass increases to 14 m, representing an 86.7% increase compared to the baseline case; When cohesion increases to 1.6 MPa, the critical safety distance can be reduced to 4.5 m, showing a 40% decrease relative to the baseline condition. These findings mechanically demonstrate the engineering value of advanced pre-grouting reinforcement technology, as enhancing surrounding rock cohesion above 1.6 MPa through pre-grouting measures can reduce the required thickness of water-resisting rock mass to within 5 m.

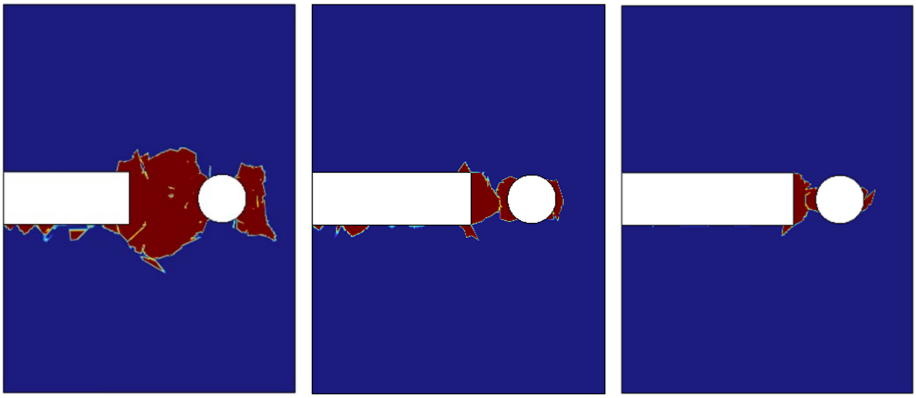

(a)C=0.8MPa, L=14m (b)C=1.2MPa, L=7.5m (c)C=1.6MPa, L=4.5m

Fig. 7. Critical Safety Distance Under Different Cohesion.

4.2 Displacement

During tunnel excavation, the displacement evolution at the tunnel face center exhibits three distinct stages (Fig. 8):

1) Stable Deformation Stage (20 m – 10 m): When the tunnel face is relatively far from the karst cave, the center displacement increases only slightly from 5.57 mm to 5.68 mm (a 1.97% increase).

2) Accelerated Deformation Stage (10 m – 7.5 m): As the excavation approaches the critical threshold, the displacement rises significantly from 5.68 mm to 7.6 mm (a 33.80% increase).

3) Catastrophic Instability Stage (<7.5 m): After breaching the safety distance, the displacement curve shows exponential divergence. Within the final 5.5 m excavation interval, displacement surges from 7.6 mm to 24.62 mm (a 223.95% increase).

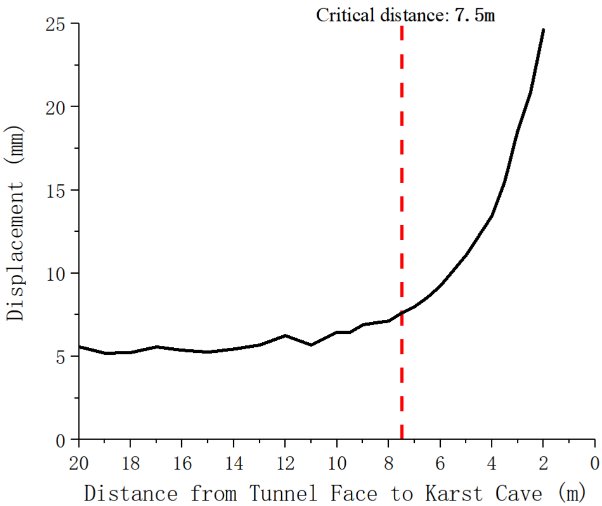

Fig. 8. Tunnel excavation distance-displacement curve.

4.3 Flow Velocity

During tunnel excavation, the distribution of the seepage velocity field exhibits significant staged changes as the distance between the tunnel face and the karst cave decreases, as illustrated in Figure 9. When the tunnel face is 20 meters away from the karst cave, the influence of the cave on the seepage field near the excavation face is relatively small, resulting in a low and relatively uniform seepage velocity. As the tunnel face approaches to 10 meters from the cave, the influence of the cave on the seepage field begins to manifest, leading to a gradual increase in seepage velocity and the onset of asymmetry in the seepage velocity field, with significantly higher velocities on the cave side. At a distance of 7.5 meters, which marks the critical safety thickness, the seepage velocity increases notably, and a distinct seepage channel forms within the rock mass between the cave and the tunnel face. When the tunnel face is just 2 meters away from the cave, the seepage velocity reaches its maximum value as the water pressure within the cave acts directly on the excavation face, creating a high-velocity seepage zone in the rock mass between the cave and the tunnel face.

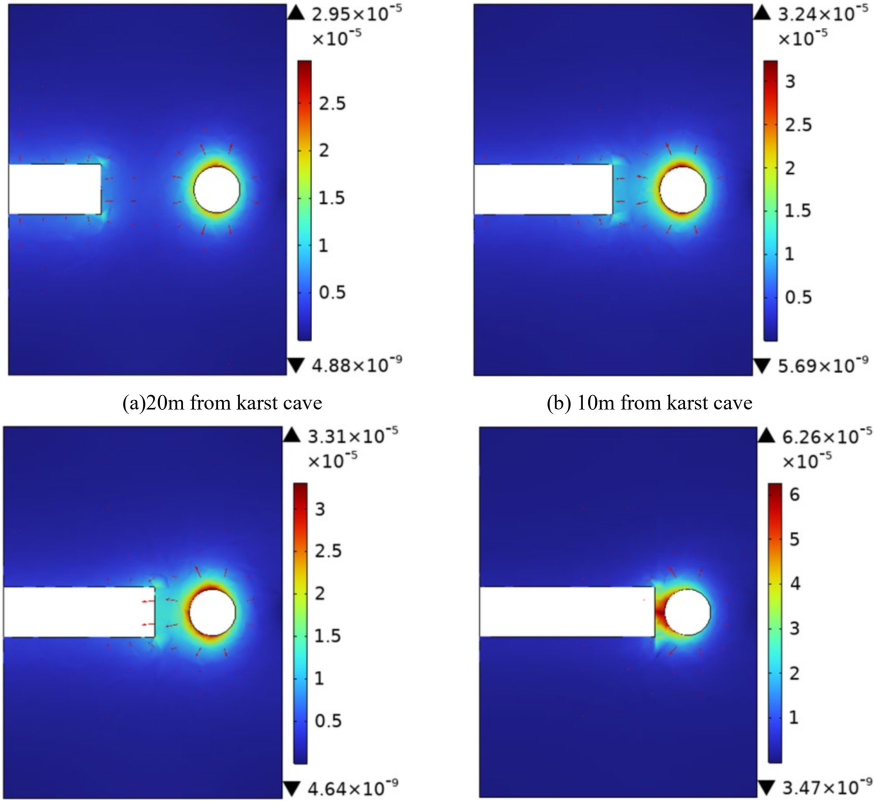

(a)20m from karst cave (b) 10m from karst cave

(c)7.5m from karst cave (d) 2m from karst cave

Fig. 9. The distribution map of seepage velocity field (m/s).

According to the simulation results, when the tunnel face is only two meters away from the karst cave, the maximum seepage velocity at the tunnel face reaches 6.26×10^{-5} m/s. Based on this, the water inflow rate at the tunnel face is calculated to be approximately 22.36 m^3 /h, which is relatively close to the initial water inflow rate of 30 m^3 /h monitored on-site at the tunnel face. Subsequently, the anti-outburst rock plate was damaged, leading to the collapse of the tunnel face and a subsequent increase in water inflow rate to 100 m^3 /h on-site.

4.4 Permeability Coefficient

The distribution of the permeability coefficient field during tunnel excavation exhibits distinct changes as the distance between the tunnel face and the karst cave decreases, as illustrated in Figure 10. According to the hypothesis of this study (Formula 7), an increase in effective stress leads to a reduction in both porosity and permeability coefficient.

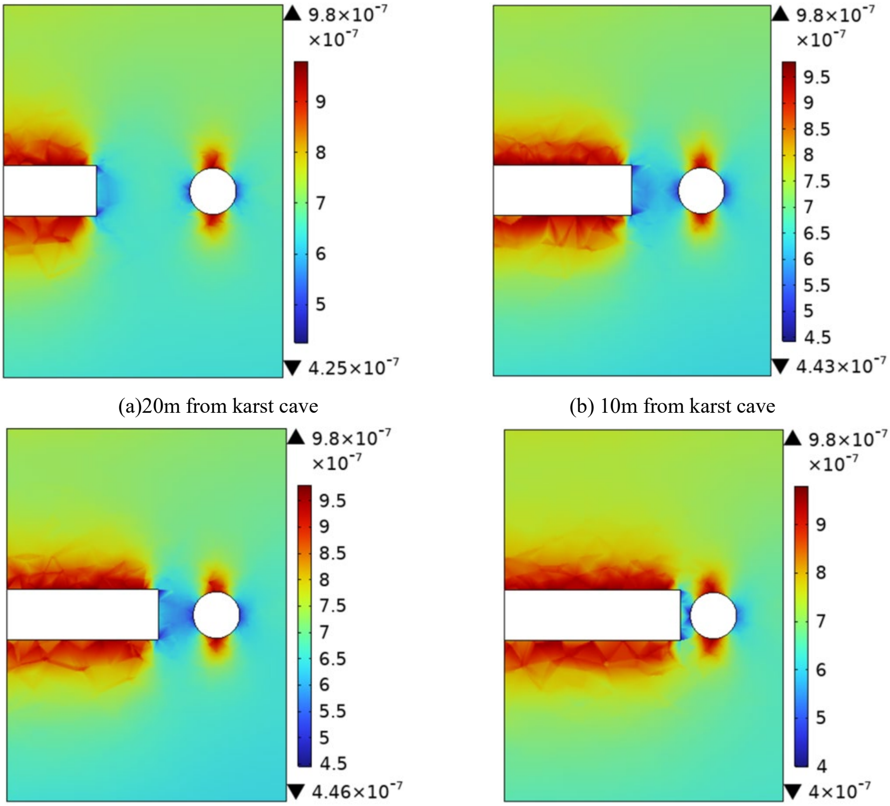

(a)20m from karst cave (b) 10m from karst cave

(c)7.5m from karst cave (d) 2m from karst cave

Fig. 10. The distribution map of permeability coefficient field (m/s).

At a distance of 20 meters from the karst cave, the minimum permeability coefficient is 4.25×10^{-7} m/s. At this stage, the anti-inrush rock plate remains intact, and the uniform distribution of effective stress maintains stable pore structures within the rock mass. The porosity remains at a relatively low level, resulting in a spatially uniform permeability coefficient field.

As the distance reduces to 10 meters, the minimum permeability coefficient slightly increases to 4.43×10^{-7} m/s. The anti-inrush rock plate begins to experience significant stress concentration, leading to non-uniform compression of pore structures due to the rising effective stress.

At the critical distance of 7.5 meters, the minimum permeability coefficient reaches its peak value of 4.46×10^{-7} m/s. Here, the anti-inrush rock plate is at a critical state of pore structure reorganization, where the pore compression effect induced by increased effective stress dynamically balances with alterations in pore connectivity.

At the distance of 2 meters, the minimum permeability coefficient decreases to 4.00×10^{-7}m/s. By this point, the anti-inrush rock plate has lost its integrity. Although the continuous increase in effective stress further compresses the matrix pores, the heterogeneous evolution of pore structures under high-stress conditions results in localized permeable pathways forming in certain areas.

5 Conclusions

This study systematically reveals the dynamic evolution patterns of the plastic zone, displacement field, seepage field, and permeability coefficient field in the surrounding rock during tunnel excavation through multi-physical field coupling analysis. Research indicates that when the tunnel face approaches 7.5 meters from the karst cave boundary, the plastic deformation zone ahead connects with the cave, forming a water inrush conduit. At this critical distance , the anti-inrush rock plate completely loses its structural integrity, establishing the minimum safety thickness threshold for karst tunnels. Displacement monitoring shows three distinct deformation stages—stable , accelerated , and catastrophic —with displacement surging exponentially after breaching the safety distance. Seepage field analysis demonstrates that seepage velocity increases significantly at 7.5 meters, forming concentrated channels, and reaches maximum values at 2 meters due to direct water pressure action. Permeability coefficient evolution exhibits a nonlinear "rise-then-fall" pattern, peaking at the critical distance due to pore structure reorganization, before decreasing as localized permeable pathways form from heterogeneous pore evolution under high stress. The study demonstrates that karst water pressure significantly impacts plastic zone development and necessitates pre-drainage measures, while rock mass cohesion critically influences critical safety distance thresholds, validating the effectiveness of pre-grouting reinforcement in reducing required water-resisting barrier thickness. These findings provide critical theoretical support for water inrush hazard warning and safety rock plate thickness design in karst tunnels.

Acknowledgments

This research was funded by a fellowship from a fellowship from the China Postdoctoral Science Foundation (no.2025M773260), a fellowship from the China Postdoctoral Science Foundation (no.2024M762779), and a fellowship from the post-doctoral innovation practice positions in Hubei province (no. 2024HBBHCXB084), the project of Key Laboratory of Water Grid Project and Regulation of Ministry of Water Resources (CX2023Z02-1).

Reference

1. Lai, Y., Li, S., Guo, J., Zhu, Z., & Huang, X. (2021). Analysis of seepage and displacement field evolutionary characteristics in water inrush disaster process of karst tunnel. Geofluids, 2021(1), 5560762.
2. Kaufmann, G., & Romanov, D. (2020). Modelling long-term and short-term evolution of karst in vicinity of tunnels. Journal of Hydrology, 581, 124282.

3. Li, Z., Wang, Y., Olgun, C. G., Yang, S., Jiao, Q., & Wang, M. (2020). Risk assessment of water inrush caused by karst cave in tunnels based on reliability and GA-BP neural network. Geomatics, Natural Hazards and Risk, 11(1), 1212-1232.
4. Xue, F., Cai, M., Wang, T., & Zhao, T. (2021). Characteristics of karst cave development in urban karst area and its effect on the stability of subway tunnel construction. Advances in Civil Engineering, 2021(1), 8894713.
5. Huang, F., Zhao, L., Ling, T., & Yang, X. (2017). Rock mass collapse mechanism of concealed karst cave beneath deep tunnel. International Journal of Rock Mechanics and Mining Sciences, 91, 133-138.
6. Xu, Z., Lin, P., Xing, H., Pan, D., & Huang, X. (2021). Hydro-mechanical coupling response behaviors in tunnel subjected to a water-filled karst cave. Rock Mechanics and Rock Engineering, 54(8), 3737-3756.
7. Lu, X., Hu, X., Xu, Z., Liao, X., Liu, L., Fu, Z., & Chen, M. T. (2022). Tunnel concealed karst cave joint detection by tunnel seismic and transient electromagnetic. Lithosphere, 2022(1).
8. Li, Z. Q., Nie, L., Xue, Y., Li, W., & Fan, K. (2025). Model Testing on the Processes, Characteristics, and Mechanism of Water Inrush Induced by Karst Caves Ahead and Alongside a Tunnel. Rock Mechanics and Rock Engineering, 1-18.
9. Ji Youjun, Liu Jianjun,Cheng Linsong. (2011). Numerieal simulation of tnnel exeavation considering fuid-solid coupling [J]. Rock and Soil Mechanics, 32(4): 1229-1231.(in chinese)
10. FU, J., WU, F., ZHANG, Y. T., & QIN, R. (2024). Interaction between Large Deformation of Surrounding Rock and Support Structure in the Soft Rock Fragmentation Section of the Qinhe Tunnel of Central Yunnan Water Diversion Project. Journal of Changjiang River Scientific Research Institute, 41(3), 171.